nature communications

Article

https://doi.org/10.1038/s41467-024-51969-4

Orientation-dependent electronic structure in interfacial superconductors $LaAlO_3/KTaO_3$

Received: 26 September 2023

Accepted: 21 August 2024

Published online: 04 September 2024

Check for updates

Xiaoyang Chen[1], Tianlun Yu[1], Yuan Liu[2], Yanqiu Sun[2], Minyinan Lei[1], Nan Guo[1], Yu Fan[1], Xingtian Sun[1], Meng Zhang[2], Fatima Alarab[3], Vladimir N. Strocov[3], Yilin Wang[4], Tao Zhou[1], Xinyi Liu[1], Fanjin Lu[1], Weitao Liu[1], Yanwu Xie[2] ✉, Rui Peng[1,5] ✉, Haichao Xu[1,5] ✉ & Donglai Feng[6,7] ✉

Emergent superconductivity at the $LaAlO_3/KTaO_3$ interfaces exhibits a mysterious dependence on the $KTaO_3$ crystallographic orientations. Here by soft X-ray angle-resolved photoemission spectroscopy, we directly resolve the electronic structure of the $LaAlO_3/KTaO_3$ interfacial superconductors and the non-superconducting counterpart. We find that the mobile electrons that contribute to the interfacial superconductivity show strong $k_\perp$ dispersion. Comparing the superconducting and non-superconducting interfaces, the quasi-three-dimensional electron gas with over 5.5 nm spatial distribution ubiquitously exists and shows similar orbital occupations. The signature of electron-phonon coupling is observed and intriguingly dependent on the interfacial orientations. Remarkably, the stronger electron-phonon coupling signature correlates with the higher superconducting transition temperature. Our observations help scrutinize the theories on the orientation-dependent superconductivity and offer a plausible and straightforward explanation. The interfacial orientation effect that can modify the electron-phonon coupling strength over several nanometers sheds light on the applications of oxide interfaces in general.

With the great success of semiconductor interfaces in electronic and photonic applications over the past 50 years, interfaces between complex oxides bring new hope for next-generation multifunctional device applications. One paradigm example is the $LaAlO_3/SrTiO_3$ (LAO/STO) interface, where the "two-dimensional electron gas" (2DEG) emerges at the interface between two band-insulators[1], and further becomes superconducting at the transition temperature (T_c) ~200 mK[2]. So far its superconducting paring mechanism remains debated[3–13]. Recently, a second family of oxide interfacial superconductors is discovered in $LaAlO_3/KTaO_3$ (LAO/KTO) and $EuO/KTaO_3$, which soon becomes a new research spotlight[14–22]. Remarkably, the superconductivity develops at T_c ~ 2 K in LAO/KTO(111)[14,15], T_c ~ 0.9 K in LAO/KTO(110)[19], but is absent in LAO/KTO(001) down to 25 mK[14]. The higher optimal-T_c than LAO/STO and the extraordinary orientation-dependent superconductivity at the KTO-based interfaces offer a new perspective for exploring the characters and mechanism of interfacial superconductivity between oxide insulators.

The orientation-dependent superconductivity has barely been observed in any other superconductors, whose origin remains a tantalizing puzzle. There are several possible explanations. First, if some

[1]Advanced Materials Laboratory, State Key Laboratory of Surface Physics, and Department of Physics, Fudan University, Shanghai, China. [2]School of Physics, Zhejiang University, Hangzhou, China. [3]Swiss Light Source, Paul Scherrer Institute, Villigen, Switzerland. [4]School of Future Technology and Department of Physics, University of Science and Technology of China, Hefei, China. [5]Shanghai Research Center for Quantum Sciences, Shanghai, China. [6]National Synchrotron Radiation Laboratory and School of Nuclear Science and Technology, New Cornerstone Science Laboratory, University of Science and Technology of China, Hefei, China. [7]School of Emerging Technology and Department of Physics, University of Science and Technology of China, Hefei, China. ✉e-mail: ywxie@zju.edu.cn; pengrui@fudan.edu.cn; xuhaichao@fudan.edu.cn; dlfeng@ustc.edu.cn

https://doi.org/10.1038/s41467-024-51969-4

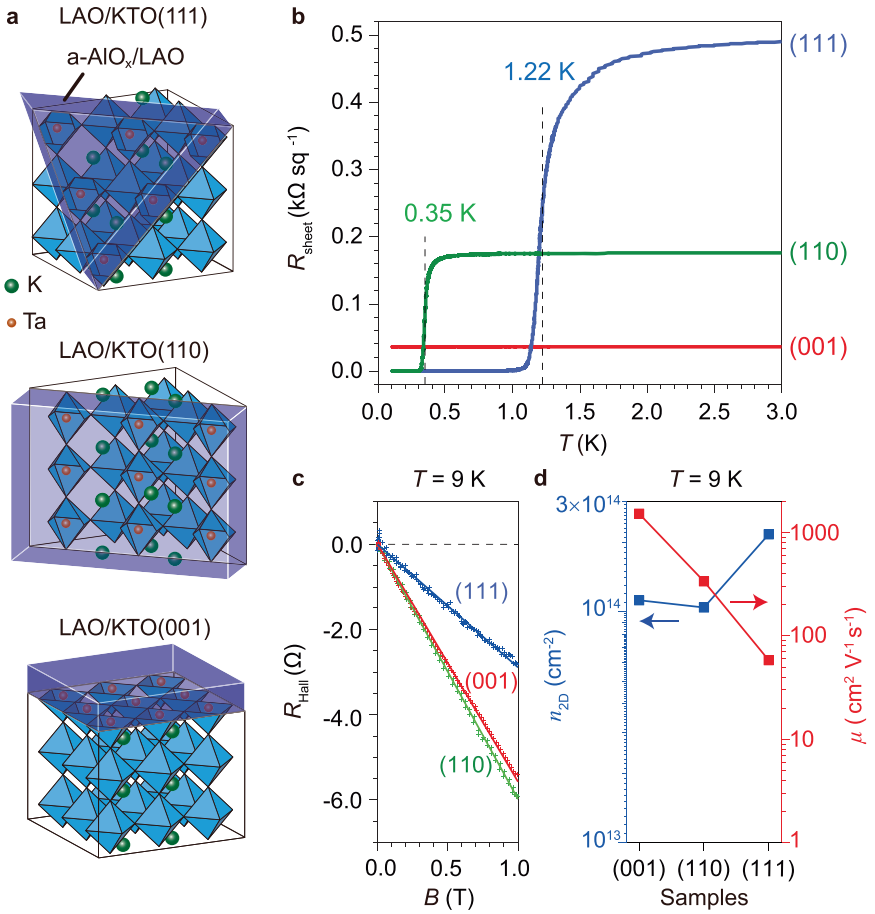

Fig. 1 | Orientation-dependent superconductivity at the LAO/KTO interfaces. **a** Sketch of the LAO/KTO interfaces with (111), (110), and (001) orientations. **b** Temperature-dependent sheet resistance (R_{sheet}) at the LAO/KTO interfaces of the three orientations. The T_c^{middle} is determined by $R_{sheet}(T_c^{middle}) = 0.5 \times R_{sheet}(3\,K)$. The lowest temperature in the measurements is 0.1 K. **c** Field-dependent Hall resistance (R_{Hall}) of the same set of samples at 9 K. **d** Two-dimensional carrier density (n_{2D}) and carrier mobility (μ) determined at the same set of samples at 9 K. n_{2D} is extracted from a linear fitting of the data in (**c**). μ is extracted from the data in (**b**) and (**c**), with $\mu^{-1} = R_{sheet} n_{2D} e$, where e is the elementary charge.

of the mobile electrons are confined to a single-interfacial layer[23,24] and are crucial to the superconductivity, the electron–phonon coupling (EPC) and interfacial superconductivity could be sensitive to the local atomic configuration at the interface[25–27]. However, this scenario seems inconsistent with the estimated superconducting layer thickness over 4 nm based on the upper critical field measurements at the KTO-based interfaces[14,15]. Secondly, pairing through inter-orbital interactions mediated by soft transverse optical (TO) phonons has been proposed to explain the superconductivity[21,28], where the orientation dependence is attributed to different orbital configurations caused by dimensional confinement[21]. In contrast to the three degenerate t_{2g} orbitals in the interfacial states of LAO/KTO(111), it is proposed that the number of occupying orbitals is reduced to two and one in LAO/KTO(110) and LAO/KTO(001), respectively, which could suppress the inter-orbital hopping and superconductivity[21]. Thirdly, the coupling between electrons and longitudinal optical (LO) phonons has been proposed to mediate superconducting pairing in LAO/STO[8,9,11–13], however, it is unclear whether/how it can cause orientation-dependent superconductivity. To examine the existing scenarios, direct measurements of the interfacial electronic states, especially the dimensionality, orbital characters, and EPC at differently oriented KTO-based interfaces are demanded.

In the superconducting LAO/KTO heterostructures, the mobile electrons are generally buried below the insulating LAO layers of over 10 nm thickness[15,19]. Only recently it is discovered that 1.5 nm-AlO$_x$/1 nm-LAO/KTO(111) retains superconductivity with the relatively thinner overlayer[29]. It is still challenging for angle-resolved photoemission spectroscopy (ARPES) measurements due to its surface sensitivity. Though the bulk-sensitive hard X-ray ARPES could reach the buried interfacial states[18], it lacks the energy/momentum resolution for inspecting the dispersive information. Here we overcome this difficulty by studying superconducting interfaces with the thinnest overlayers and exploiting ~1000 eV-photon-excited soft X-ray (SX-) ARPES with adequate probing depth and decent energy/momentum resolution[30,31], which is demonstrated as a powerful tool in determining the dimensionality of interfacial electronic states[32]. Our results show the quasi-three-dimensional electronic structure of the interfacial states in both superconducting and non-superconducting interfaces. On the other hand, the observed spectral signature of EPC, which is between the interfacial mobile electrons and surface phonons of KTO, is strikingly orientation-dependent and correlates with the superconductivity.

Results

Transport properties

Amorphous overlayers were grown on top of KTO with (111), (110), and (001) orientations (Fig. 1a) using pulsed laser deposition[29]. With the optimized overlayer of 1.5 nm-AlO$_x$/1 nm-LAO/KTO, the temperature dependence of the sheet resistance (R_{sheet}) shows superconducting transitions with T_c^{middle} = 1.22 K and 0.35 K for (111) and (110) orientations, respectively (Fig. 1b). As for the (001) orientation, the superconducting transition is not observed down to 0.1 K. Two-terminal resistance of 3 nm-LAO/KTO show T_c^{middle} = 1.3 K, 0.7 K, and <0.4 K for LAO/KTO(111),

LAO/KTO(110), and LAO/KTO(001), respectively (Supplementary Note 1). Although the T_c is slightly lower than LAO/KTO with thicker LAO[15,19], the orientation dependence of $T_c(111) > T_c(110) > T_c(001)$ persists, in both AlO_x/LAO/KTO and LAO/KTO. The two-dimensional carrier density (n_{2D}) at 9 K was extracted from the field-dependent Hall resistance (Fig. 1c), as summarized in Fig. 1d. According to the superconducting phase diagrams of electrical gate tuned EuO/KTO(111)[16] and EuO/KTO(110)[21], our samples locate at the optimal n_{2D} region. The electron mobility (μ) at 9 K is determined from the corresponding n_{2D} and R_{sheet}, showing $\mu(111) < \mu(110) < \mu(001)$ (Fig. 1d). For LAO/KTO(111), the perpendicular and parallel upper critical fields are measured. The superconducting layer thickness (d_{SC}) and the superconducting coherence length (ξ) can be estimated by upper critical fields based on the Ginzburg-Landau theory[33], giving $\xi_{\parallel} \sim 20$ nm and $d_{SC} \sim 5$ nm (Supplementary Note 2). The superconducting coherence length larger than the superconducting thickness suggests the two-dimensional superconductivity at the LAO/KTO(111) interfaces, which is consistent with previous studies[14,15]. These transport properties indicate that our samples of different orientations host the typical characters of LAO/KTO interfaces despite the reduced thickness of the insulating overlayers.

Dimensionality of the interfacial states

As shown in Fig. 2a, the interfaces were well grounded by AlSi-wire and silver paste for SX-ARPES measurements. The momentum-integrated energy distribution curve (EDC) of LAO/KTO(111) shows a peak near E_F, accompanied by a shoulder around −2 eV attributed to oxygen vacancy states[34] (Fig. 2b). These vacancies are reported to arise during LAO deposition and are intrinsic to the interfacial state[29]. The peak near E_F indicates metallic interfacial states in contrast to its insulating components. Notably, the EDCs exhibit consistent characteristics throughout the measurement process, with minimal variation observed during photon irradiation (Supplementary Note 3). This behavior is distinct from the irradiation-induced metallic states at the KTO surfaces[34–37], demonstrating the interfacial origin of the mobile electrons. The density of states (DOS) at E_F is prominently contributed by dispersive features (Fig. 2c–j), suggesting that the interfacial mobile electrons accumulate at the crystalline KTO side rather than at the amorphous LAO side.

Intriguingly, in stark contrast to a pure two-dimensional state, the measured interfacial electronic structure is highly dispersive along $k_\perp$ ($k_{[111]}$ for LAO/KTO(111)) (Fig. 2c–e). Specifically, the peak positions of the momentum distribution curves (MDCs) integrated around E_F vary along $k_\perp$ (Fig. 2e), and the changes of the Fermi velocity at different $k_\perp$ further demonstrate the existence of $k_\perp$ dispersion rather than intensity variation (Supplementary Note 4). Together with the Fermi momenta (k_Fs) determined based on the major/minor axis of the elongated Fermi surfaces (blue-filled markers in Fig. 2d, see Supplementary Note 5 for details on determining k_Fs), they consistently form

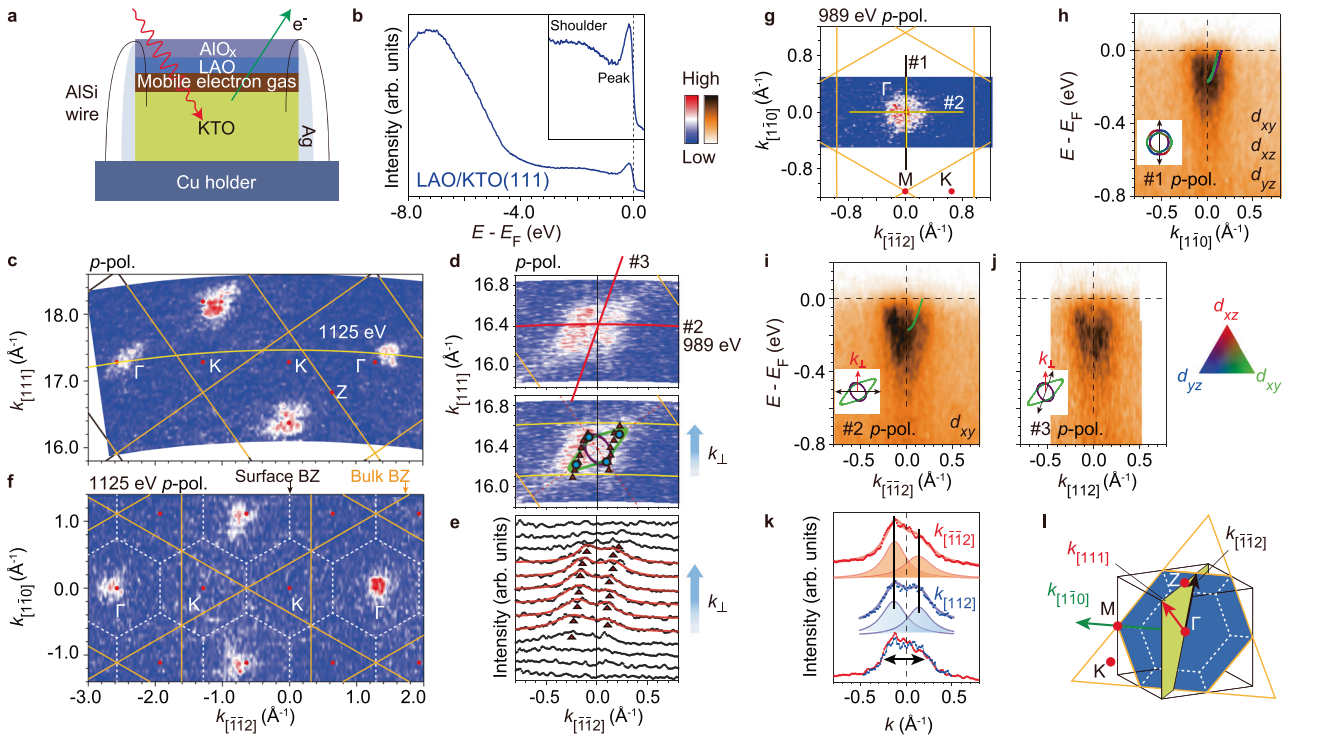

Fig. 2 | Quasi-three-dimensional characters of the mobile electronic states at the LAO/KTO(111) interface. a Sketch of the sample mounting and grounding for SX-ARPES measurements. **b** The momentum-integrated energy distribution curve (EDC) of LAO/KTO(111). The inset shows the zoomed-in view near the E_F. **c**, **d** Out-of-plane photoemission intensity maps integrated over [E_F − 150 meV, E_F + 150 meV] in $k_{[\bar{1}\bar{1}2]}$-$k_{[111]}$ plane using *p*-polarized (*p*-pol.) photons. The photon energies range from 950 to 1280 eV in (**c**) and from 921 to 1044 eV in (**d**). In the lower part of (**d**), the triangles mark the peak positions of the momentum distribution curves (MDCs) in (**e**), and the circles mark the k_Fs that are determined based on the major/minor axis of the ellipsoid Fermi surface. The blue and purple curves illustrate the Fermi surfaces. **e** MDCs integrated over [E_F − 150 meV, E_F + 150 meV] of the spectra measured at different photon energies, whose $k_\perp$ locations are illustrated in the lower part of (**d**). The MDCs are fitted by two Lorentzian peaks and a linear background to determine the k_Fs. **f**, **g** In-plane photoemission intensity maps integrated over [E_F − 150 meV, E_F + 150 meV] using 1125 and 989 eV photons, respectively. The corresponding $k_\perp$ locations are marked in (**c**) and (**d**). **h**–**j** Photoemission spectra along cuts #1 ($k_{[1\bar{1}0]}$), #2 ($k_{[\bar{1}\bar{1}2]}$), and #3 ($k_{[112]}$), respectively. spectra in (**j**) is extracted from the map data in (**d**). The corresponding momentum locations are marked in (**d**) and (**g**). The calculated electron-doped bulk KTO bands are overlaid on the right side after a chemical potential shift to match the experimental k_Fs and the orbital characters are noted. The insets show the calculated Fermi surfaces and specify the direction of the cuts. **k** MDCs integrated over [E_F − 150 meV, E_F + 150 meV] of spectra in (**i**) and (**j**). **l** Sketch of KTO bulk Brillouin zone, zone boundaries from truncation at the (111) plane (orange solid line), and the surface Brillouin zone (white dashed line). Some related high symmetric directions are indicated.

a closed Fermi surface contour (Fig. 2d). The in-plane Fermi surfaces also follow the periodicity of the bulk Brillouin zones (orange solid lines in Fig. 2f) rather than the two-dimensional Brillouin zones of the surface atomic layer (white dashed lines in Fig. 2f). Along two equivalent cuts of the in-plane $k_{[\bar{1}\bar{1}2]}$ (cut #2, Fig. 2i) and the dominantly out-of-plane $k_{[112]}$ (cut #3, Fig. 2j) in the bulk Brillouin zone, the photoemission spectra show similar features. The MDCs near E_F are also identical in width (Fig. 2k). Such accordance indicates that the out-of-plane momentum broadening, which combines the effects from the thickness confinement of interfacial states and the photoemission probing depth[38], is comparable to the in-plane momentum resolution, further demonstrating the quasi-three-dimensionality of the electronic states.

Based on the Luttinger theorem[39], the carrier density (n_{3D}) can be extracted according to the Fermi surface volume (Supplementary Note 5). Considering inhomogeneous doping in different depth at oxide interfaces[40,41], the n_{3D} from ARPES should represent the portions of higher carrier dopings. Therefore the thickness estimated by $d_{e,min} = n_{2D}/n_{3D}$, where n_{2D} is determined by Hall resistance measurements, can represent a lower limit of the spatial distribution of the interfacial mobile electrons. n_{3D} and $d_{e,min}$ are estimated to be 3.2×10^{20} cm^{-3} and 6.8 nm for LAO/KTO(111) interfacial states, respectively (Supplementary Note 5). We also resolved the interfacial electronic states in LAO/KTO(110) and LAO/KTO(001) samples, and all the interfacial states show quasi-three-dimensional character (Supplementary Note 4). The same analysis gives $d_{e,min}$ of 6.0 nm and 5.5 nm for LAO/KTO(110) and LAO/KTO(001), respectively (Supplementary Note 5), which are at the same scale as that of LAO/KTO(111). Such a wide confined region of the electron gas would result in three-dimensional electronic structures and a strong $k_\perp$ dispersion as shown in the simulations of the extended quantum well scenario[32,38,42], which are consistent with our experimental observations.

It is reported that the spatial distribution of interfacial charge carriers in LAO/STO is significantly affected by the oxygen vacancies[43]. Compared with previous SX-ARPES results on LAO/STO, the highly dispersive electronic structure of LAO/KTO along $k_\perp$ direction is distinct from that of in-situ oxygen-annealed LAO/STO, while similar to that of oxygen-deficient LAO/STO interface[32], which is consistent with the presence of oxygen vacancy states[29] (Fig. 2b). The quasi-three dimension character of the electron gas does not violate the reported two-dimensional superconductivity in LAO/KTO[14,15], as the superconducting thickness of the same sample is determined to be much smaller than the superconducting coherence length (Supplementary Note 2). The lower limit of the electron gas thickness $d_{e,min}$ is comparable to the superconducting thickness. Considering the superconducting thickness of 5 nm, the critical ingredients that lead to the orientation-dependent superconductivity at the interface should be active at tens of unit cells near the interface.

Orbital composition of the interfacial states

The orbital composition of the electronic states can be compared at differently orientated interfaces to scrutinize the orbital-related pairing scenario[21]. The photoemission intensity maps of LAO/KTO(110), LAO/KTO(001), and LAO/KTO(111) all show Fermi surfaces extending along the Γ–X, Γ–Y, and Γ–Z directions (Figs. 3a, b and 2d). The elongated Fermi surface lobes at three perpendicular directions agree well with the expected Fermi surface sheets of electronic bands formed by Ta t_{2g} orbitals (d_{xy}, d_{xz}, d_{yz}) (Fig. 3c)[44]. As depicted in Fig. 3d for the d_{yz} orbital, the overlaps with neighboring d_{yz} are smaller along x direction than those along y and z directions, resulting in a heavy band mass and a larger k_F along Γ–X direction as shown by the theoretical calculations (Fig. 3e). Similarly, d_{xz} and d_{xy} orbitals show heavy band mass and elongation of Fermi surfaces along Γ–Y and Γ–Z directions, respectively. Considering that the Ta t_{2g} orbitals are further hybridized by spin–orbital coupling, we conducted the density functional theory (DFT) calculations on bulk KTO, and the calculated band structure roughly agrees with the experiments upon a chemical potential shift (Figs. 2h, i, 3f–k). Note that there are minor differences that might be caused by finite interfacial confinement (Supplementary Note 6); however, the differences are much less conspicuous than those between bulk KTO and KTO surface 2DEG[35,37], consistent with the larger thickness of the interfacial states observed in LAO/KTO.

Polarization-dependent ARPES measurement is a powerful tool to identify orbital characters[45,46] (the observable orbitals are noted on the right part in Figs. 3f–k, 2h, i, see detailed analysis in Supplementary Note 7). Combining the data from both p-polarized and s-polarized geometries, all the three t_{2g} orbitals are identified in LAO/KTO(110) (Fig. 3f–h) and LAO/KTO(001) (Fig. 3i–k), suggesting no change in the number of occupying orbitals as compared with those in LAO/KTO(111) (Fig. 2h, i). These experimental observations exclude a significant difference in orbital occupation numbers among differently-orientated LAO/KTO interfaces, which is consistent with the thick electron gas and minor effect of dimensional confinement at the interfaces. These results disfavor the direct relation between orientation-dependent superconductivity and orbital occupations[21].

Orientation-dependent spectral weight tail

The high symmetry direction M–Γ–M ($k_{[1\bar{1}0]}$) in the bulk Brillouin zone is an equivalent in-plane momentum cut for three interfaces with (111), (110), and (001) orientations (Fig. 4a), along which the photoemission spectra of three samples can be well compared to explore the origin of the orientation-dependent superconductivity (Fig. 4b–d). It is important to note that even with the confinement of 1–2 nm thickness, the lowest-lying bands of the KTO surface 2DEGs show negligible modifications in the in-plane effective mass along $k_{[1\bar{1}0]}$[35–37], and the confinement over 5.5 nm thickness in LAO/KTO should give even less change. Therefore, a rigid chemical potential shift of the DFT-calculated bulk bands by aligning the k_F should give a reliable band bottom for the bare band. For LAO/KTO(111), the bottom of t_{2g} conduction band is expected at binding energy $E_B \simeq 0.17$ eV, and consistently the peak positions of EDCs support an occupied bandwidth less than 0.2 eV (Supplementary Note 8). However, the photoemission spectral weight extends far beyond the calculated band bottom (Fig. 4b–d), with a long tail down to E_B ~ 0.4 eV for LAO/KTO(111) (Fig. 4d). Intriguingly, LAO/KTO(111) has the most prominent spectral tail (Fig. 4d), followed by LAO/KTO(110) (Fig. 4c), and LAO/KTO(001) the least (Fig. 4b). This difference in spectral weight tail at differently-oriented interfaces can be observed both in the raw spectral image (Fig. 4b–d), in the momentum-integrated EDCs (black curves in Fig. 4h–j) and in the EDCs at k_F (black curves in Fig. 4k–m). Specifically, the EDC peak is the sharpest in LAO/KTO(001) (Fig. 4h), while much broader in LAO/KTO(110) and LAO/KTO(111) (Fig. 4i, j), showing an orientation dependence.

Discussion

We have presented the similarities and differences in the interfacial electronic structure of LAO/KTO across three different interface orientations: the consistent presence of a quasi-three-dimensional electron gas with a distribution range of 5–7 nm at the interfaces, accompanied by similar t_{2g} orbital occupations, and the different spectral weight tails with orientation dependence. The dimensionality and orbital occupation underscore the uniformity and robustness of the electronic structure at differently oriented interfaces. On the other hand, the different spectra weight tail introduces a novel orientation-dependent aspect of the KTO-based interfaces. Understanding this phenomenon can provide insights into the possible origin of the intriguing orientation-dependent superconductivity.

In SX-ARPES, the dominant effect of disorder scatterings is converting the coherent dispersive spectra weight into the incoherent non-dispersive background, while the energy broadening of spectral function is relatively minor[47]. The spectral tails observed at higher binding energies retain the momentum distribution of bands near the

https://doi.org/10.1038/s41467-024-51969-4

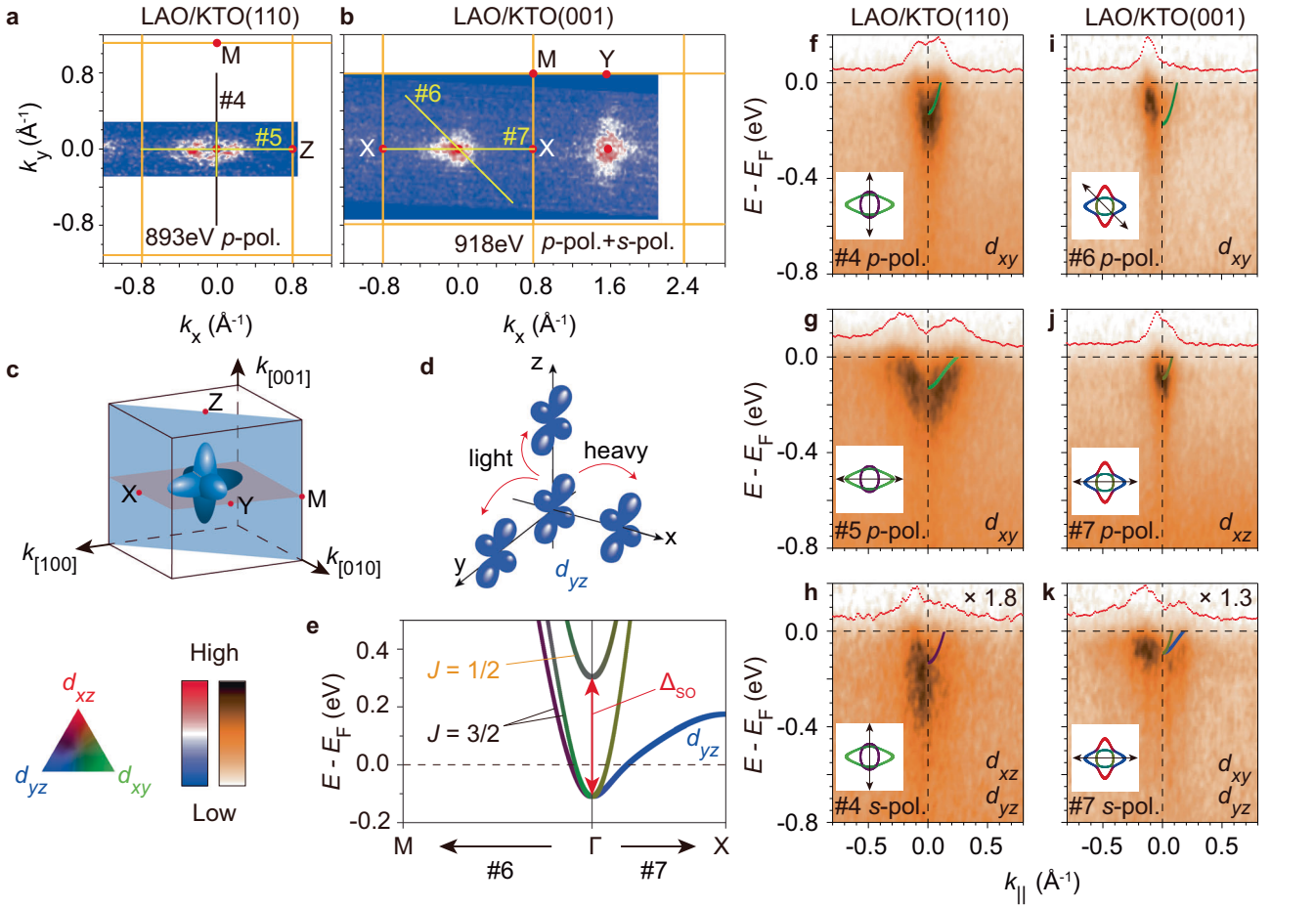

Fig. 3 | Interfacial electronic structure of LAO/KTO(110) and LAO/KTO(001). **a**, **b** In-plane photoemission intensity maps across Γ of LAO/KTO(110) and LAO/KTO(001), respectively. The intensity is integrated over [E_F − 150 meV, E_F + 150 meV]. **c** Sketch of the ellipsoid-like Fermi surfaces of the electron-doped KTO and truncating planes of (110) and (001). **d** Sketch of the electron hopping between neighboring d_{yz} orbitals. **e** Calculated band dispersions of the electron-doped bulk KTO along M–Γ–X. The spin–orbital coupling in KTO mixes the three t_{2g} orbitals and lifts the J = 1/2 band up by ~0.4 eV. It leaves two J = 3/2 bands crossing the E_F to form the double-layer Fermi surfaces, while the extremal parts of the extended lobes retain the nearly single orbital character of the corresponding t_{2g} orbital, as shown for d_{yz}. **f**–**k** Photoemission spectra along cuts #4, #5, #6, and #7. The corresponding momentum locations are marked in (**a**) and (**b**). MDCs integrated between [E_F − 35 meV, E_F + 35 meV] are overlaid on the top of each panel. The calculated electron-doped bulk KTO bands are overlaid on the right side after a chemical potential shift to match the experimental k_Fs and the orbital characters are noted. The insets show the calculated Fermi surfaces and specify the direction of the cuts. Data from *s*-polarized geometry, which are strongly suppressed owing to matrix element effect[69], are amplified by a factor in (**h**) and (**k**).

Fermi energy, suggesting that they are unlikely induced by secondary electrons or disorder scattering from random scattering processes. Electron correlation is not likely a cause either, as it usually reduces the bandwidth rather than enlarges it[48,49]. A plausible explanation for the spectral tail is the shaking off of phonon quanta due to electron coupling with small-q phonons[7–9].

Due to the insufficient resolution of SX-ARPES with ~1000 eV photons, the peak-dip-hump structure with the separated main band and replicas by phonon energy could not be resolved (Supplementary Note 9). Note that superconductivity has recently been achieved at the KTO surfaces under electric gating, displaying a similar orientation dependence as the interface[50,51]. Therefore, as a supplement, we studied the spectral weight tail on KTO(110) surface using VUV-ARPES with much better energy resolution, where the peak-dip-hump structure can indeed be resolved, showing an energy separation between the peak and hump around 100 meV (Supplementary Fig. 15). Assuming that the spectral weight tail observed in LAO/KTO is the combination of quasiparticle peaks and their shake-off replicas by 100 meV phonons, the relative intensity among different replica bands should follow Poisson distribution according to the Franck-Condon model. Consistently, the EDCs can be well-fitted by the Franck-Condon model, which works as a semi-quantitative estimation of the EPC strength. Note that the slight variations in band filling attributing to different carrier concentrations have already been considered in the fitting (see details in Supplementary Note 8 and Supplementary Note 13). Such fitting also gives $\lambda(111) > \lambda(110) > \lambda(001)$. The relative spectra weight of the main band (blue shade in Fig. 4h–j), shows orientation dependence, with $Z(111) < Z(110) < Z(001)$, and a similar trend has recently been reported at the KTO surface as well[52]. Note that the scenario of extrinsic energy loss of emitted photoelectrons[53] can be excluded considering the high kinetic energy of the photoelectrons in our experiments (Supplementary Note 10). The electron–phonon coupling can shorten the lifetime of the quasiparticle, thereby increasing the normal state resistivity and reducing the mobility, which likely explains the differences in normal state resistance and mobility in differently-orientated LAO/KTO with $R_{sheet}(111) > R_{sheet}(110) > R_{sheet}(001)$ (Fig. 1b) and $\mu(111) < \mu(110) < \mu(001)$ (Fig. 1d). The EPC coupling strength with $\lambda(111) > \lambda(110) > \lambda(001)$ coincides with that of the superconductivity with $T_c(111) > T_c(110) > T_c(001)$, providing a plausible explanation for the orientation-dependent superconductivity.

Concerning the origin of the 100 meV phonons, their energy is close to that of the LO4 bulk phonons[54–57] and LO4-derived Fuchs-

https://doi.org/10.1038/s41467-024-51969-4

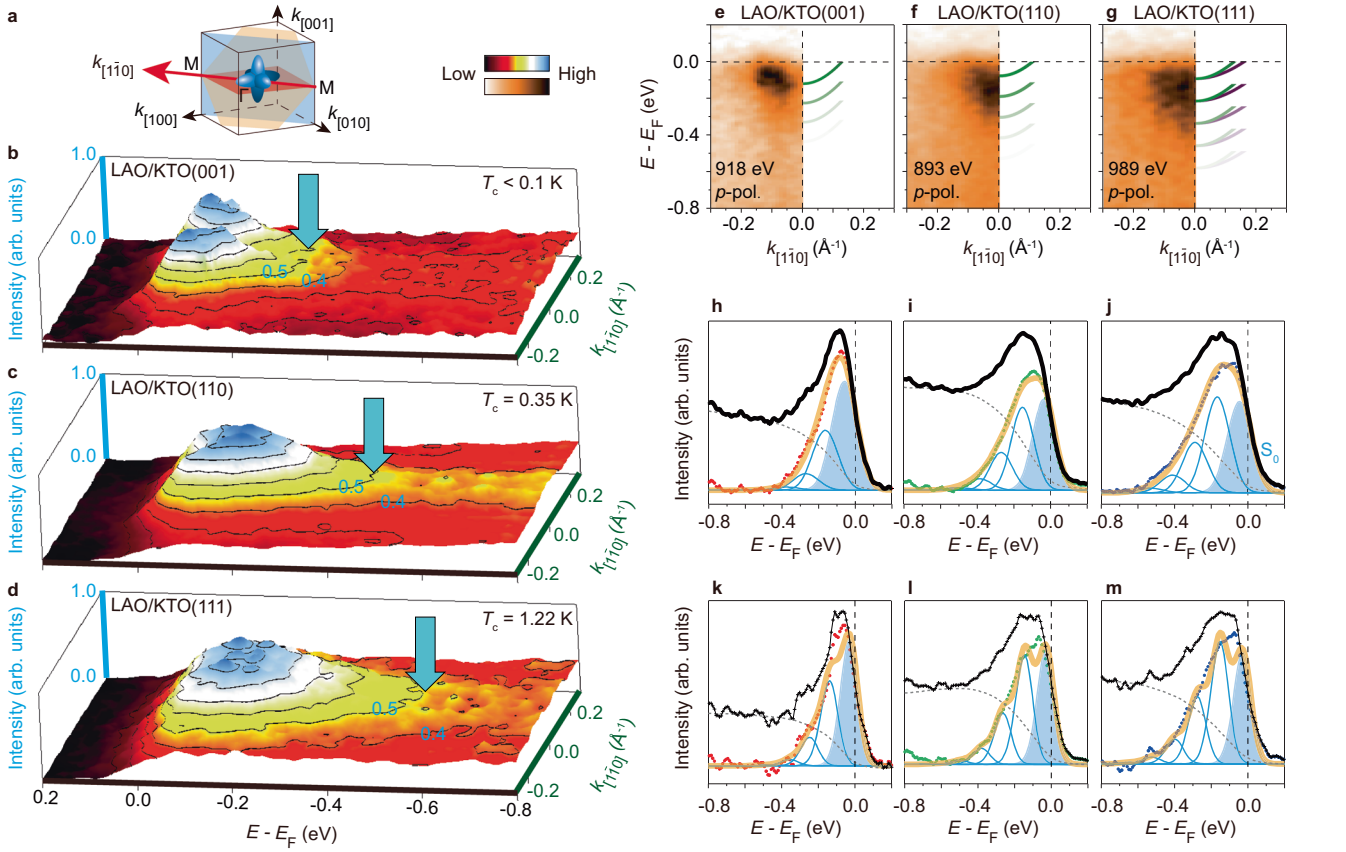

Fig. 4 | Orientation-dependent electron–phonon coupling at the LAO/KTO interfaces. a Sketch of the in-plane truncations of the KTO bulk Brillouin zone at the (111) plane (orange), (110) plane (blue), and (001) plane (red). The cut along $k_{[1\bar{1}0]}$ (Γ–M) is specified. **b**–**d** Three-dimensional plots of photoemission spectra along $k_{[1\bar{1}0]}$ of LAO/KTO(001), (110), and (111), respectively. Data were measured at 19 K using *p*-polarized photons. The photons with energies of 918 eV, 893 eV, and 989 eV, which cut the Γ points of LAO/KTO(001), (110), and (111), respectively, were used in the measurements. The photoemission intensities are normalized by the maximum in (**b**–**d**) and the contour lines are appended. Blue arrows at contour lines of 0.5 specify the spectral weight tails. **e**–**g** Photoemission spectra in (**b**–**d**) (left side) and the renormalized main band and its replicas accounting for electron–phonon coupling (right side). The transparency of bands indicates their relative intensity based on fitting the EDCs in (**h**–**j**). **h**–**j** EDCs integrated over [−0.3 Å^{-1}, 0.3 Å^{-1}] of the spectra in (**b**–**d**). EDCs are fitted by the Franck-Condon model after subtracting the Tougaard backgrounds (gray dashed curves), which are commonly used for inelastically scattered electrons[70–72]. Similar results can be obtained by subtracting an incoherent and dispersionless background of EDCs (Supplementary Note 12). The bandwidth and energy separation of the main band and replicas are renormalized by the EPC[73,74] (Supplementary Note 13). The blue shade (S_0) represents the density of states contributed by the main band in the fittings. **k**–**m** EDCs at k_F of the spectra in (**b**–**d**). The EDCs are fitted by the Franck-Condon model as the analysis in (**h**–**j**), while the spectra weight of the main band and replica bands are represented by Gaussians considering Fermi-Dirac distribution and energy resolution (Supplementary Note 13).

Kliewer surface phonons (see HR-EELS results in Supplementary Note 11). Given that superconductivity is absent in chemically doped bulk KTO[58,59], EPC with the bulk phonons, if present, should be less crucial for the superconductivity, while further investigations are required to understand this. Among the surface phonons, Fuchs-Kliewer surface phonon mode is known to be long-range, especially at small wave vector q, with amplitude decaying exponentially into the bulk by e^{-qd} (d is the distance away from the surface or interface[60]). Decay length of several tens of nanometers was reported in the Fuchs-Kliewer modes of polar semiconductors[61–64]. Therefore, there should be a prominent spatial overlap between the depth scale of the small q Fuchs-Kliewer modes at the LAO/KTO interface and the observed quasi-three-dimensional and nanometer-thick interfacial electronic states, which allows their coupling and can explain the observed spectral weight tails. Phonon-mediated superconducting pairing in LAO/KTO is consistent with the recent superfluid stiffness measurements suggesting a nodeless superconducting order parameter at the AlO_x/KTO(111) interface[20]. Surface Fuchs-Kliewer phonons could be sensitive to sample surfaces; for instance, the different polar strength among the three KTO interfaces and the induced lattice relaxation may modify the Fuchs-Kliewer modes and their coupling with the electrons. While the detailed variation among crystalline orientations and how it induces the observed orientation-dependent electron–phonon coupling encourage future theoretical development.

To summarize, our results demonstrate the weak dimensional confinement and the similar orbital characters at the interfaces of differently-orientated LAO/KTO, which help scrutinize the theories of orientation-dependent superconductivity. Meanwhile, the tuning parameter of superconductivity in LAO/KTO is likely the coupling between the interfacial mobile electrons and the Fuchs-Kliewer phonons of KTO with small q. The measured Fermi surfaces and possible electron–phonon coupling behavior in our study can provide experimental foundations for constructing theories describing electron–phonon coupling and the orientation-dependent superconductivity in LAO/KTO. Furthermore, our observation suggests that interfacial orientations can affect electron–phonon coupling strength over several nanometers, which could provide new routes for engineering various functional properties that are closely related to electron–phonon coupling, including ferroelectricity, multiferroism, and superconductivity.

Methods

Sample fabrication

Amorphous $LaAlO_3$ (LAO) and $AlO_x/LaAlO_3$ (AlO_x/LAO) were grown on (111)-, (110)-, and (001)-oriented single crystalline $KTaO_3$ (KTO) substrates (MTI Corporation) by pulsed laser deposition (PLD) using a 248-nm KrF excimer laser. During the growth, substrates were heated to 650–680 °C in a mixed atmosphere of 1×10^{-5} mbar O_2 and 1×10^{-7} mbar H_2O vapor following previous report[29]. The laser fluence was ~1 J cm^{-2} and the repetition rate was 2 Hz for both LAO and AlO_x.

Transport measurements

The temperature-dependent electrical resistivity and Hall resistivity were performed using a physical properties measurement system (PPMS, Quantum Design, Inc.). For all the measurements, the excitation current was 1 μA.

ARPES measurements

ARPES measurements were performed at Advanced Resonant Spectroscopies (ADRESS) beamline in Swiss Light Source, Paul Scherrer Institute, Switzerland. To avoid the photoemission charging effect, the conducting interfaces were grounded by AlSi wire to copper sample holder using ultrasonic wire bonding. Samples were heated to 250 °C for half an hour before ARPES measurements to remove the surface adsorbates owing to air-exposure, and such low-temperature annealing is not expected to induce oxygen vacancies in KTO[37]. Data were collected by a PHOIBIOS 150 (SPECS) analyzer with 840–1280 eV photons under an ultra-high vacuum of 2×10^{-11} mbar. Photon flux was about 10^{13} photons/s, and the beam spot was 30 × 75 μm^2. The measurements were conducted at 19 K. The overall energy resolution is ~140 meV, and the angular resolution was 0.1°.

HR-EELS measurements

HR-EELS measurements were conducted on the single crystal KTO substrates of (111)-, (110)-, and (001)-crystallographic orientations (MTI Corporation). Clean surfaces were obtained by annealing at ~680 °C in an ultra-high vacuum of 5×10^{-9} mbar for 45 min. RHEED and LEED patterns were collected to verify the surface quality before HR-EELS measurements. The incident electron beam in HR-EELS measurements is produced by an electron gun of Model LK5000M (LK Technologies). The incident electron energy was 13.6 eV and the incident angle with respect to the surface normal was 45°. Data were collected by an analyzer A-1 (MBS) under an ultra-high vacuum of 5×10^{-11} mbar. The measurements were conducted at 295 K.

Theoretical calculations

Density functional theory (DFT) calculation of bulk $KTaO_3$ was performed by the open source Quantum Espresso (QE) code[65,66]. The exchange-correlation potential is treated within the generalized gradient approximation (GGA) of the Perdew-Burke-Ernzerhof variety[67]. The strong spin-orbit coupling of Ta is included in the calculation. The kinetic energy cutoffs for wave functions and charge density are set to be 80 Ry and 800 Ry, respectively. Integration for the Brillouin zone is done using a Γ-centered $11 \times 11 \times 11$ k-point grid. A tight-binding (TB) Hamiltonian consisting of six Ta-t_{2g} orbitals (including spin) is constructed using the Wannier90 package[68]. The Fermi surface is then computed based on this TB Hamiltonian.

Data availability

Relevant data supporting the key findings of our study are available within the article and the Supplementary Information file. All raw data generated during our current study are available from the corresponding authors upon request. Source data are provided with this paper.

References

1. Ohtomo, A. & Hwang, H. A high-mobility electron gas at the $LaAlO_3$/$SrTiO_3$ heterointerface. *Nature* **427**, 423–426 (2004).
2. Reyren, N. et al. Superconducting interfaces between insulating oxides. *Science* **317**, 1196–1199 (2007).
3. Gastiasoro, M. N., Ruhman, J. & Fernandes, R. M. Superconductivity in dilute $SrTiO_3$: a review. *Ann. Phys.* **417**, 168107 (2020).
4. Wölfle, P. & Balatsky, A. V. Superconductivity at low density near a ferroelectric quantum critical point: Doped $SrTiO_3$. *Phys. Rev. B* **98**, 104505 (2018).
5. Enderlein, C. et al. Superconductivity mediated by polar modes in ferroelectric metals. *Nat. Commun.* **11**, 4852 (2020).
6. Van der Marel, D., Barantani, F. & Rischau, C. Possible mechanism for superconductivity in doped $SrTiO_3$. *Phys. Rev. Res.* **1**, 013003 (2019).
7. Cancellieri, C. et al. Polaronic metal state at the $LaAlO_3$/$SrTiO_3$ interface. *Nat. Commun.* **7**, 10386 (2016).
8. Wang, Z. et al. Tailoring the nature and strength of electron-phonon interactions in the $SrTiO_3$(001) 2D electron liquid. *Nat. Mater.* **15**, 835–839 (2016).
9. Chen, C., Avila, J., Frantzeskakis, E., Levy, A. & Asensio, M. C. Observation of a two-dimensional liquid of Fröhlich polarons at the bare $SrTiO_3$ surface. *Nat. Commun.* **6**, 8585 (2015).
10. Meevasana, W. et al. Strong energy-momentum dispersion of phonon-dressed carriers in the lightly doped band insulator $SrTiO_3$. *N. J. Phys.* **12**, 023004 (2010).
11. Geondzhian, A. et al. Large polarons as key quasiparticles in $SrTiO_3$ and $SrTiO_3$-based heterostructures. *Phys. Rev. Lett.* **125**, 126401 (2020).
12. Gor'kov, L. P. Phonon mechanism in the most dilute superconductor *n*-type $SrTiO_3$. *Proc. Natl Acad. Sci. USA* **113**, 4646–4651 (2016).
13. Klimin, S., Tempere, J., Devreese, J. & Van Der Marel, D. Interface superconductivity in $LaAlO_3$-$SrTiO_3$ heterostructures. *Phys. Rev. B* **89**, 184514 (2014).
14. Liu, C. et al. Two-dimensional superconductivity and anisotropic transport at $KTaO_3$(111) interfaces. *Science* **371**, 716–721 (2021).
15. Chen, Z. et al. Electric field control of superconductivity at the $LaAlO_3$/$KTaO_3$(111) interface. *Science* **372**, 721–724 (2021).
16. Qiao, W. et al. Gate tunability of the superconducting state at the EuO/$KTaO_3$(111) interface. *Phys. Rev. B* **104**, 184505 (2021).
17. Rubi, K. et al. Electronic subbands in the *a*-$LaAlO_3$/$KTaO_3$ interface revealed by quantum oscillations in high magnetic fields. *Phys. Rev. Res.* **3**, 033234 (2021).
18. Zapf, M. et al. Hard x-ray angle-resolved photoemission from a buried high-mobility electron system. *Phys. Rev. B* **106**, 125137 (2022).
19. Chen, Z. et al. Two-dimensional superconductivity at the $LaAlO_3$/$KTaO_3$(110) heterointerface. *Phys. Rev. Lett.* **126**, 026802 (2021).
20. Mallik, S. et al. Superfluid stiffness of a $KTaO_3$-based two-dimensional electron gas. *Nat. Commun.* **13**, 4625 (2022).
21. Liu, C. et al. Tunable superconductivity and its origin at $KTaO_3$ interfaces. *Nat. Commun.* **14**, 951 (2023).
22. Arnault, E. G. et al. Anisotropic superconductivity at $KTaO_3$(111) interfaces. *Sci. Adv.* **9**, eadf1414 (2023).
23. Sing, M. et al. Profiling the interface electron gas of $LaAlO_3$/$SrTiO_3$ heterostructures with hard X-ray photoelectron spectroscopy. *Phys. Rev. Lett.* **102**, 176805 (2009).
24. Cancellieri, C. et al. Interface Fermi states of $LaAlO_3$/$SrTiO_3$ and related heterostructures. *Phys. Rev. Lett.* **110**, 137601 (2013).
25. Peng, R. et al. Picoscale structural insight into superconductivity of monolayer FeSe/$SrTiO_3$. *Sci. Adv.* **6**, eaay4517 (2020).
26. Song, Q. et al. Evidence of cooperative effect on the enhanced superconducting transition temperature at the FeSe/$SrTiO_3$ interface. *Nat. Commun.* **10**, 758 (2019).

27. Li, Z. et al. Molecular beam epitaxy growth and post-growth annealing of FeSe films on $SrTiO_3$: a scanning tunneling microscopy study. *J. Phys.: Condens. Matter* **26**, 265002 (2014).
28. Gastiasoro, M. N., Temperini, M. E., Barone, P. & Lorenzana, J. Theory of superconductivity mediated by Rashba coupling in incipient ferroelectrics. *Phys. Rev. B* **105**, 224503 (2022).
29. Sun, Y. et al. Critical thickness in superconducting $LaAlO_3$/$KTaO_3$(111) heterostructures. *Phys. Rev. Lett.* **127**, 086804 (2021).
30. Strocov, V. et al. Soft-X-ray ARPES facility at the ADRESS beamline of the SLS: concepts, technical realisation and scientific applications. *J. Synchrotron Radiat.* **21**, 32–44 (2014).
31. Strocov, V. et al. High-resolution soft X-ray beamline ADRESS at the Swiss Light Source for resonant inelastic X-ray scattering and angle-resolved photoelectron spectroscopies. *J. Synchrotron Radiat.* **17**, 631–643 (2010).
32. Strocov, V. et al. Dimensionality of mobile electrons at x-ray-irradiated $LaAlO_3$/$SrTiO_3$ interfaces. *Electron. Struct.* **4**, 015003 (2022).
33. Kozuka, Y. et al. Two-dimensional normal-state quantum oscillations in a superconducting heterostructure. *Nature* **462**, 487–490 (2009).
34. King, P. et al. Subband structure of a two-dimensional electron gas formed at the polar surface of the strong spin-orbit perovskite $KTaO_3$. *Phys. Rev. Lett.* **108**, 117602 (2012).
35. Santander-Syro, A. et al. Orbital symmetry reconstruction and strong mass renormalization in the two-dimensional electron gas at the surface of $KTaO_3$. *Phys. Rev. B* **86**, 121107 (2012).
36. Bareille, C. et al. Two-dimensional electron gas with six-fold symmetry at the (111) surface of $KTaO_3$. *Sci. Rep.* **4**, 3586 (2014).
37. Bruno, F. Y. et al. Band structure and spin–orbital texture of the (111)-$KTaO_3$ 2D electron gas. *Adv. Electron. Mater.* **5**, 1800860 (2019).
38. Moser, S. et al. How to extract the surface potential profile from the ARPES signature of a 2DEG. *J. Electron Spectrosc. Relat. Phenom.* **225**, 16–22 (2018).
39. Luttinger, J. Fermi surface and some simple equilibrium properties of a system of interacting fermions. *Phys. Rev.* **119**, 1153 (1960).
40. Scopigno, N. et al. Phase separation from electron confinement at oxide interfaces. *Phys. Rev. Lett.* **116**, 026804 (2016).
41. Strocov, V. et al. Electronic phase separation at $LaAlO_3$/$SrTiO_3$ interfaces tunable by oxygen deficiency. *Phys. Rev. Mater.* **3**, 106001 (2019).
42. Strocov, V. Photoemission response of 2D electron states. *J. Electron Spectrosc. Relat. Phenom.* **229**, 100–107 (2018).
43. Basletic, M. et al. Mapping the spatial distribution of charge carriers in $LaAlO_3$/$SrTiO_3$ heterostructures. *Nat. Mater.* **7**, 621–625 (2008).
44. Santander-Syro, A. et al. Two-dimensional electron gas with universal subbands at the surface of $SrTiO_3$. *Nature* **469**, 189–193 (2011).
45. Zhang, Y. et al. Out-of-plane momentum and symmetry-dependent energy gap of the pnictide $Ba_{0.6}K_{0.4}Fe_2As_2$ superconductor revealed by angle-resolved photoemission spectroscopy. *Phys. Rev. Lett.* **105**, 117003 (2010).
46. Xu, H. et al. Electronic structure of the $BaTi_2As_2O$ parent compound of the titanium-based oxypnictide superconductor. *Phys. Rev. B* **89**, 155108 (2014).
47. Della Valle, E., Constantinou, P., Schmitt, T., Aeppli, G. & Strocov, V. N. Static disorder in soft X-ray angle-resolved photoemission spectroscopy: theory and application to ion-bombarded InAs(110). Preprint at https://arxiv.org/abs/2308.03707 (2023).
48. Sobota, J. A., He, Y. & Shen, Z.-X. Angle-resolved photoemission studies of quantum materials. *Rev. Mod. Phys.* **93**, 025006 (2021).
49. Yi, M. et al. Bandwidth and electron correlation-tuned superconductivity in $Rb_{0.8}Fe_2(Se_{1-z}S_z)_2$. *Phys. Rev. Lett.* **115**, 256403 (2015).
50. Ueno, K. et al. Discovery of superconductivity in $KTaO_3$ by electrostatic carrier doping. *Nat. Nanotechnol.* **6**, 408–412 (2011).
51. Ren, T. et al. Two-dimensional superconductivity at the surfaces of $KTaO_3$ gated with ionic liquid. *Sci. Adv.* **8**, eabn4273 (2022).
52. Xu, H. et al. Giant tunability of Rashba splitting at cation-exchanged polar oxide interfaces by selective orbital hybridization. *Adv. Mater.* **36**, 2313297 (2024).
53. Li, F. & Sawatzky, G. A. Electron phonon coupling versus photoelectron energy loss at the origin of replica bands in photoemission of FeSe on $SrTiO_3$. *Phys. Rev. Lett.* **120**, 237001 (2018).
54. Vogt, H. & Uwe, H. Hyper-Raman scattering from the incipient ferroelectric $KTaO_3$. *Phys. Rev. B* **29**, 1030 (1984).
55. Vogt, H. Hyper-Raman tensors of the zone-center optical phonons in $SrTiO_3$ and $KTaO_3$. *Phys. Rev. B* **38**, 5699 (1988).
56. Perry, C. et al. Phonon dispersion and lattice dynamics of $KTaO_3$ from 4 to 1220 K. *Phys. Rev. B* **39**, 8666 (1989).
57. Jandl, S., Banville, M., Dufour, P., Coulombe, S. & Boatner, L. Infrared study of oxygen vacancies in $KTaO_3$. *Phys. Rev. B* **43**, 7555 (1991).
58. Wemple, S. Some transport properties of oxygen-deficient single-crystal potassium tantalate ($KTaO_3$). *Phys. Rev.* **137**, A1575 (1965).
59. Thompson, J., Boatner, L. & Thomson, J. Very low-temperature search for superconductivity in semiconducting $KTaO_3$. *J. Low. Temp. Phys.* **47**, 467–475 (1982).
60. Fuchs, R. & Kliewer, K. Optical modes of vibration in an ionic crystal slab. *Phys. Rev.* **140**, A2076 (1965).
61. Li, L., Tindall, C., Takaoka, O., Hasegawa, Y. & Sakurai, T. Structural and vibrational properties of 6H-SiC (0001) surfaces studied using STM/HREELS. *Surf. Sci.* **385**, 60–65 (1997).
62. Späth, T., Becker, D., Schulz, N., Hausbrand, R. & Jaegermann, W. Understanding the SEI formation at pristine Li-Ion cathodes: chemisorption and reaction of DEC on $LiCoO_2$ surfaces studied by a combined SXPS/HREELS approach. *Adv. Mater. Interfaces* **4**, 1700567 (2017).
63. Nienhaus, H., Kampen, T. & Mönch, W. Phonons in 3C-, 4H-, and 6H-SiC. *Surf. Sci.* **324**, L328–L332 (1995).
64. Dubois, L. & Schwartz, G. Surface optical phonons and hydrogen chemisorption on polar and nonpolar faces of GaAs, InP, and GaP. *Phys. Rev. B* **26**, 794 (1982).
65. Giannozzi, P. et al. QUANTUM ESPRESSO: a modular and open-source software project for quantum simulations of materials. *J. Phys.: Condens. Matter* **21**, 395502 (2009).
66. Giannozzi, P. et al. Advanced capabilities for materials modelling with Quantum ESPRESSO. *J. Phys.: Condens. Matter* **29**, 465901 (2017).
67. Perdew, J. P., Burke, K. & Ernzerhof, M. Generalized gradient approximation made simple. *Phys. Rev. Lett.* **77**, 3865 (1996).
68. Mostofi, A. A. et al. An updated version of wannier90: a tool for obtaining maximally-localised Wannier functions. *Comput. Phys. Commun.* **185**, 2309–2310 (2014).
69. Moser, S. An experimentalist's guide to the matrix element in angle resolved photoemission. *J. Electron Spectrosc. Relat. Phenom.* **214**, 29–52 (2017).
70. Tougaard, S. Quantitative analysis of the inelastic background in surface electron spectroscopy. *Surf. Interface Anal.* **11**, 453–472 (1988).
71. Tougaard, S. Practical guide to the use of backgrounds in quantitative XPS. *J. Vac. Sci. Technol. A* **39**, 011201 (2021).
72. Liu, C. et al. High-order replica bands in monolayer FeSe/$SrTiO_3$ revealed by polarization-dependent photoemission spectroscopy. *Nat. Commun.* **12**, 4573 (2021).
73. Li, Z.-X., Devereaux, T. & Lee, D.-H. Electronic and phononic properties of a two-dimensional electron gas coupled to dipolar phonons via small-momentum-transfer scattering. *Phys. Rev. B* **100**, 241101 (2019).

74. Marsiglio, F. Eliashberg theory: a short review. *Ann. Phys.* **417**, 168102 (2020).

Acknowledgements

This work is supported in part by the National Natural Science Foundation of China (Grants Nos. 12274085 (to R.P.), 12074074 (to H.C.X.), 11922403 (to R.P.), 11934016 (to Y.W.X.)), the National Key R&D Program of the MOST of China (2023YFA1406300 (to H.C.X. and R.P.)), the Shanghai Municipal Science and Technology Major Project (Grant No. 2019SHZDZX01 (to R.P. and H.C.X.)), the New Cornerstone Science Foundation (to D.L.F.), and the Innovation Program for Quantum Science and Technology (Grant No. 2021ZD0302803 (to D.L.F.)). We thank Dr. Xiaoxiao Wang and Suppanut Sangphet for their valuable advice during the preparation of the manuscript and for their support in measuring supplemental data. The experiments have been performed at the SX-ARPES endstation of the ADRESS beamline at the Swiss Light Source, Paul Scherrer Institute, Switzerland. Some preliminary data at the beginning of the project were taken at the BL09U ARPES endstation of the Shanghai Synchrotron Radiation Facility, and some supplementary data were taken at the QMSC beamline of the Canadian Light Source.

Author contributions

Y.L., Y.Q.S., X.Y.C., N.G., M.Z., and Y.W.X. prepared the samples and conducted transport measurements. T.L.Y., X.Y.C., F.A., V.S., and N.G. conducted ARPES measurements. X.Y.C., N.G., Y.F., M.Y.N.L., and X.T.S. conducted HR-EELS measurements. T.Z., X.Y.L., F.J.L., and W.T.L. conducted sum-frequency generation spectroscopy measurements. Y.L.W. conducted DFT calculations. X.Y.C., R.P., H.C.X., and N.G. analyzed the ARPES and HR-EELS data. R.P., X.Y.C., H.C.X., and D.L.F. wrote the paper. Y.W.X., R.P., H.C.X., and D.L.F. are responsible for project direction and planning. All the authors discussed the experiments and calculation results.

Competing interests

The authors declare no competing interests.

Additional information

Supplementary information The online version contains supplementary material available at https://doi.org/10.1038/s41467-024-51969-4.

Correspondence and requests for materials should be addressed to Yanwu Xie, Rui Peng, Haichao Xu or Donglai Feng.

Peer review information *Nature Communications* thanks Andres Santander-Syro, Zhiming Wang, and the other, anonymous, reviewer(s) for their contribution to the peer review of this work. A peer review file is available.